Crystal and Electronic Structure of Bismuth Thiophosphate, $BiPS_4$: An Earth Abundant Solar Absorber

Devendra Tiwari[a,†], Dominic Alibhai[b], David Cherns[c] and David J Fermin[a,*]

[a]School of Chemistry, University of Bristol, Bristol – BS8 1TS, UK

[b]Wolfson Bioimaging Facility, Faculty of Biomedical Sciences,

University of Bristol, University Walk, Bristol BS8 1TD, UK

[c]H.H. Wills Physics Laboratory, University of Bristol, Tyndall Av., Bristol BS8 1TL. United Kingdom

*david.fermin@bristol.ac.uk

Abstract

The opto-electronic properties of crystalline $BiPS_4$ are described for the first time for solar energy conversion. Detailed structural-analysis is extracted from XRD refinement of powders synthesized by solid-state method. $BiPS_4$ exhibits a rather unusual 3-dimensional orthorhombic structure with two distinctive Bi sites with octahedral coordination distorted by $6s^2$ lone-pairs. High-resolution TEM imaging clearly shows the two Bi-Bi interatomic distances in close agreement with the XRD analysis. $BiPS_4$ displays a complex Raman spectrum under near-resonant conditions which is rationalized by Density Functional Perturbation Theory. Hybrid-functional-DFT calculations show significant spin-orbit-coupling effects in Bi-6p bands, affecting not only on the band dispersion but also lowering the conduction band minimum by approximately 0.5 eV. Optical properties of $BiPS_4$ powders are dominated by a direct transition at 1.72 eV, closely matching the calculated band gap. Electrochemical experiments revealed n-type conductivity with a flat band potential located at 0.16 V vs RHE. We also show a remarkable agreement between the position of the band edges estimated from first-principles calculations and electrochemical measurements. Time-resolved Photoluminescence transient revealed a carrier-lifetime of approximately 1 ns, manifesting as strong potential and wavelength dependent photocurrent responses. Finally, the nature of structural defects responsible for the relatively short lifetime is briefly discussed.

†current address: Department of Mathematics, Physics and Electrical Engineering, Northumbria University, Newcastle upon Tyne, NE1 8ST, United Kingdom

1. Introduction

Semiconductor materials based on Bi^{+3} cations are receiving increasing attention as potential solar absorbers for photovoltaic (PV) applications due to their unique relativistic properties, Earth abundancy and low toxicity.[1–3] In principle, Bi^{+3} can induce some of the attractive optoelectronic properties observed in Pb^{2+} hybrid perovskite, such as broad-band dispersion, large Born effective charges, high dielectric constant, spin-orbit effects and defect-tolerance.[4] A variety of Bi-materials have been implemented in a diverse range of applications including catalysis,[5] photocatalysis,[6] thermoelectrics[7], topological insulators,[8] ferroelectrics,[9] photodetectors[10] and superconductors.[11] In the context of solar absorbers, a variety of bismuth compounds have been investigated such as chalcogenides (Bi_2S_3, $CuBiS_2$, $AgBiS_2$),[12,13] halides (BiI_3, $AgBiI_4$, $AgBi_2I_7$, $Cs_3Bi_2I_9$, $CH_3NH_3)_3Bi_2I_9$)[14–21] oxyhalides (BiOI, BiOCl)[22–24], chalcohalides (BiSI)[23,25], and, Inorganic perovskite ($BiFeO_3$)[26].

Chalcophosphates with a general formula of $A^{m+}[P_xCh_y]^{n-}$ (Ch = S, Se) are semiconductor materials with a wide range of structure diversity, displaying ferroelectric, non-linear optoelectronic and photoconductive response in near-infrared to ultraviolet region.[27–36,32,37] Structure complexity becomes even more pronounced with a heavy partially-oxidised cation such as Bi^{+3}, due to the possible stereochemical activity of the ns^2 lone-pair.[37–39] For example, Bi^{+3} chalcogenides can form prismatic,[40] trigonal-pyramidal,[41] and square-pyramidal,[42] coordination. Similar trends have been observed in a wide range of bismuth chalcophosphates.[37,42–44]

In this report, we provide the first in-depth analysis of $BiPS_4$ as a solar absorber, combining detailed crystal structure analysis on $BiPS_4$ powder, first-principles DFT calculations and photoelectrochemical measurements. The complex bonding patterns and symmetry of this fascinating yet poorly understood material is elucidated by quantitative structure refinement of X-ray diffraction patterns, high-resolution electron microscopy and near-resonant Raman spectroscopy. DFT studies illustrate the effect of spin-orbit coupling on the band structure and band gap of $BiPS_4$, which is fully consistent with diffuse reflectance measurements. We combine optical, electrochemical and electronic structure calculations to establish the band edge positions, the type majority carriers (electrons) and the character of the orbitals associated with the conduction and valence band edges. Photoelectrochemical studies and time-resolved photoluminescence measurements show that, despite the high degree of crystallinity and fulfilling the main criteria for defect-tolerance, carrier lifetime in the range of 1 ns.

2. Methods

2.1 Synthesis. $BiPS_4$ is prepared by solid-state reaction inspired by procedures reported elsewhere,[45,46] in which stoichiometric amounts of elemental bismuth, red phosphorus and sulphur are sealed in quartz ampoule evacuated to a pressure < 1 x 10^{-6} mbar under Ar atmosphere. The reaction was first heated to 860 ^{o}C (i.e. above the melting point of Bi_2S_3) at a rate of 5 ^{o}C/min and dwelled for 24 hours. Thereafter, the reaction was allowed to cool down to 680 ^{o}C (just above the melting point of $BiPS_4$) and to dwell for 96 hours, before naturally cooling down to room temperature. The as-grown material is black and crystalline, which was first washed with dimethylformamide, rinsed with methanol and dried overnight at room temperature under rotary vacuum.

2.2 Characterization and photoelectrochemical studies. Powder X-ray diffraction was acquired using a Bruker D8 advance diffractometer fitted with Cu Kα source and a position-sensitive Lynxeye detector. High-angle annular dark-field (HADDF) imaging was carried out in an aberration-corrected scanning transmission electron microscope (STEM) - JEOL ARM200F fitted with a cold field emission source, capable of reaching to probe the size of <0.1 nm. The sample was prepared from a dispersion of finely ground powder in methanol, on to a holey carbon grid. Scanning electron micrographs were collected using a JEOL iT300 microscope in secondary electron detection mode. Energy-dispersive X-ray spectrum (EDX) is measured after exciting the carbon-coated sample with 20 keV electron beam using an Oxford X-max 80 mm^2 silicon drift detector fitted in the same electron microscope. Prior to the EDX measurements, the sample was coated with 20 nm of Carbon film, deposited by vacuum evaporation, to prevent sample charging. Raman spectrum of the sample was measured with a Renishaw inVia spectrometer upon exciting the sample with a 785 nm diode laser. The spectrometer employs a bandpass filter to clip the Rayleigh scattering and inhibits acquisition below 85 cm^{-1}. Diffuse reflectance spectroscopy of a $BiPS_4$ powder was performed using a Shimadzu UV-2600 UV-Vis spectrometer in a wavelength range of 500 nm to 850 nm. The diffuse reflectance measurements are performed against the $BaSO_4$ as a reflectance standard. $BaSO_4$ was also been used as an effectively zero-background dilutant for the sample (10% $BiPS_4$ + 90% $BaSO_4$).

$BiPS_4$ thin films were prepared by mulling powder with ethanol in an agate mortar pestle to form a thick uniform slurry which was cast on FTO coated glass substrates using doctor blade technique. Electrochemical measurements were performed in argon saturated 0.1 M Na_2SO_3 electrolyte (pH 6.5) with a Pt counter and Ag/AgCl reference electrodes. The Ag/AgCl potential (U) scale was converted to reversible hydrogen electrode (RHE) scale using the relationship: U (V vs RHE) = U (V vs Ag/AgCl) + 0.197 V + (0.059 x pH) V and the 0 V (vs RHE) was considered to be at 4.44 eV vs Vacuum. To obtain the capacitance-voltage data, electrochemical impedance spectra of the $BiPS_4$ electrodes were measured in 0.5 M Na_2SO_4

electrolyte (pH 6.8) in the frequency range of 7 to 5700 Hz with 13 mV AC modulation using Solatron Modulab system. Photoelectrochemical measurements were performed with quartz halogen lamp and a Bentham TM300 monochromator fitted with mechanical chopper operating at 27 Hz. The photon flux at each wavelength was calibrated a Si photodiode from Newport Corporation. Photocurrent responses were measured with a Stanford Research System lock-in amplifier (SRS 830) coupled to an Ivium technologies compactstat potentiostat. The data acquisition was enabled by a custom interface written in National Instrument's LabVIEW. Time-resolved photoluminescence measurements are performed using TCSPC (time-correlated single-photon counting) system as incorporated in a TCS SP8 system coupled to a Leica DMi8 inverted microscope (Leica Microsystems). The emission decay is collected from 52 x 52 μm area after 633 nm excitation at 25 ^{o}C for 309s with 4ps bin.

2.3 Computational methods. Geometry optimization of $BiPS_4$ unit cell is performed with CASTEP code.[47,48] Strict iteration tolerance of 1 x 10^{-9} eV/atom and 0.001 eV/Å were enforced for energy and force convergences, respectively. Calculations are performed with GGA-PBE functional with Grimme dispersion correction,[49] On-the-fly norm-conserving pseudopotentials with energy cut-off of 400 eV and Monkhorst-Pack grid with a spacing of 0.02 $Å^{-1}$ was employed for k-point sampling. Calculations of the Raman spectrum was carried under density functional perturbation (DFPT) linear response formalism. The DFT functional was switched to hybrid HSE06 for the electronic structure calculation with and without spin-orbit coupling while using zero-order regular approximation (ZORA) scheme to include relativistic effects of Bi.[50] The ionization potential (IP) was calculated using a slab-gap model and performing electrostatic potential calculations with GGA-PBE functional.[51]

3. Results and Discussion

3.1 Structure and composition of $BiPS_4$ particles. A representative energy dispersive analysis of X-ray (EDX) spectrum of an ensemble of $BIPS_4$ crystals is displayed in **Figure 1a**, while the elemental mapping of a crystal is illustrated in **Figure S1**. The contribution of the main elements can be quantitively resolved, providing an accurate estimation of the composition ratio, while the elemental map (**Figure S1**) confirms a homogenous distribution of the elements at the individual particle level. The Bi, P and S ratios estimated from the spectrum are 16.47 ± 0.25, 16.23 ± 0.20, and 67.33 ± 0.21 (atomic) %, respectively, which corresponds to a stoichiometry of 0.99:0.97:4.04. **Figure 1b** shows the powder X-ray diffraction (XRD) pattern of the $BiPS_4$ in the range of 15^{o} to 70^{o}, exhibiting the characteristic features of an orthorhombic crystal structure with Ibca symmetry. The standard ICSD pattern shown in **Figure S2**, based on the crystal structure reported by Zimmerman et al.,[45] confirms that no significant peaks are observed below 15^{o}. A full profile quantitative structural refinement using the Rietveld method resulted in a highly accurate fit as illustrated by the red continuous line in the XRD and the residual line (blue trace) across the diffraction range in **Figure 1b**. The statistical correlation parameters R_p and R_{wp} of the fit were 4.68% and 6.0%, respectively, and no peaks associated with secondary phases or alternative ternary compositions are observed. $BiPS_4$ is found to crystallize in an unit cell with lattice parameters of around a = 10.5945(9.5) Å, b = 11.1138(9.9) Å and c = 19.6595(17.9) Å.

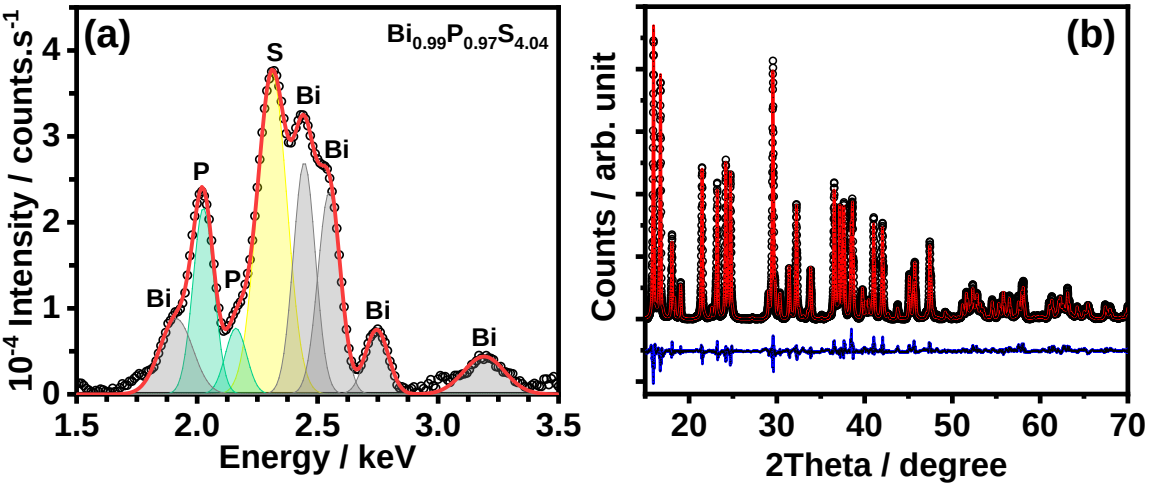

Figure 1. Compositional and structural analysis: (a) Energy-dispersive X-ray spectrum showing the contribution from all three elements. (b) Powder X-ray diffraction (XRD) and structure refinement based on the Rietveld method.

Figure 2 illustrates the complex structural motif associated with $BiPS_4$, while additional observations have been included in the supporting information. The $BiPS_4$ unit cell is illustrated in **Figure 2a**, highlighting the distorted octahedral coordination of the Bi atoms and the two Bi-Bi interatomic distances, which are clearly seen in the atomic resolution dark-field STEM image in **Figure 2b**. A rectangular array of Bi columns is observed rotated by approximately 7° clockwise (see inset in **Figure 2b**). To the best of our knowledge, is the first atomic-scale image of a material of the main-group chalcophosphate class. The Bi-Bi distances measured along the vertical and horizontal directions are 5.6 Å and 5.3 Å, in close agreement with the Bi-Bi distances estimated from XRD refinement (5.61 Å and 5.36 Å, respectively). It should be mentioned that contrast in dark-field imaging varies to the square of atomic number (Z), thus given the large Z difference between Bi (83) and S (16) and P (15), it is rather challenging to image the P and S columns. As shown in **Figure 2c**, Bi atoms have two different coordinations, Bi(1) bonded to 6 S atoms in distorted octahedron coordination and Bi(2) is bonded to 8 S atoms with four S atoms arranged in a rectangular fashion. The significant distortion from the regular polyhedral angles, by up to ~40°, is indicative of a stereochemically active $6s^2$ lone-pair on Bi sites, which have also been observed in Bi compounds such as Bi_2S_3 and $K_2Bi_8Se_{13}$.[41] **Figure 2d** shows the 2-dimensional view of the bonding in the (010) plane, illustrating the Bi-S and P-S polyhedral, while **Figure 2e** illustrates how the S atoms arranged in chains of edge-sharing tetrahedrons along the [100] and [010] directions which inter-transform by a diad screw axis along the [001] direction.

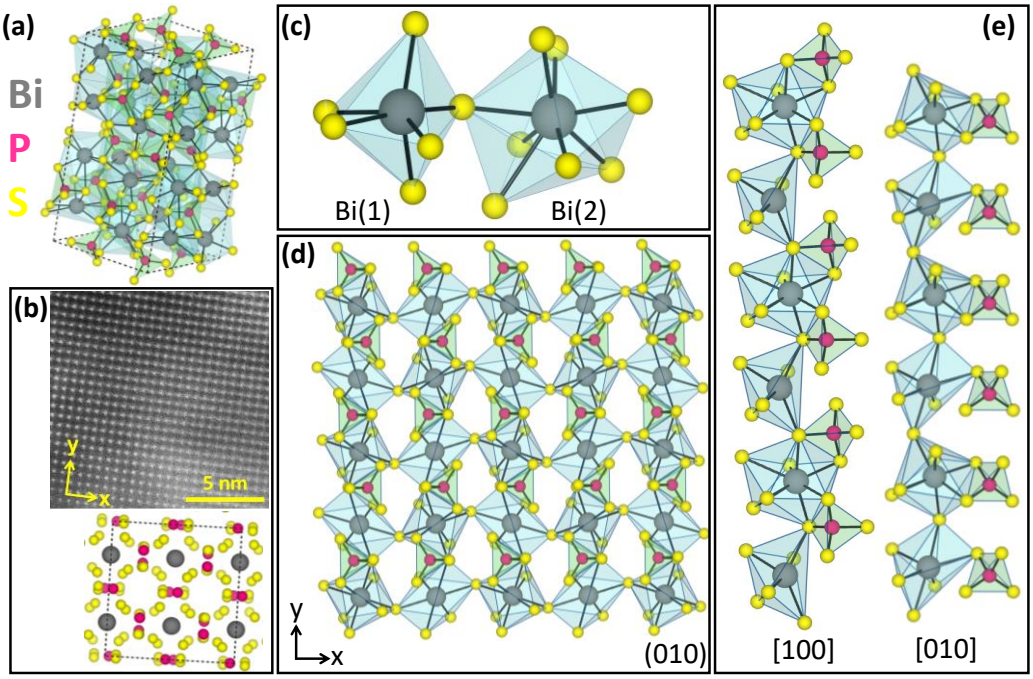

Figure 2. Structure and bonding in $BiPS_4$: (a) Schematic of the unit cell elucidated by the XRD analysis; (b) HAADF-STEM image of showing the two characteristic Bi-Bi interatomic distances as represented by the projection of the unit cell. Schematic representations of (c) the two distinctive Bi-S polyhedral, (d) Bi-S and P-S polyhedra along (010) plane and (d) network of S atoms around Bi and P atoms along the [100] and [010].

As shown in **Table 1**, our XRD structural analysis is highly consistent with previous structural analysis on single crystals reported by Zimmermann et al.,[45] with differences in lattice parameters well below 0.1%. The crystallographic information file of refined structure can also be obtained from the CCDC/FIZ Karlsruhe repository (deposition number: 1961688). **Table 1** also includes the lattice parameters obtained by unit cell optimization using DFT with PBE functional and Grimme dispersion corrections (see **2.3 Computational methods**). The excellent agreement of optimized structures and experimental crystallographic analysis provides a solid platform for the modelling phonon modes and electronic structure described further below.

Table 1. Lattice parameters extracted from the XRD analysis and cell optimization by DFT. The values are compared to lattice parameters previously reported for single crystals.

	Single Crystal§	Powder XRD	DFT
a (Å)	10.601	10.595 (-0.06 %)	10.645 (+0.415%)
b (Å)	11.112	11.114 (+ 0.016 %)	11.144 (+0.288%)
c (Å)	19.661	19.66 (-0.008%)	19.647 (-0.071 %)

§Obtained from reference 45

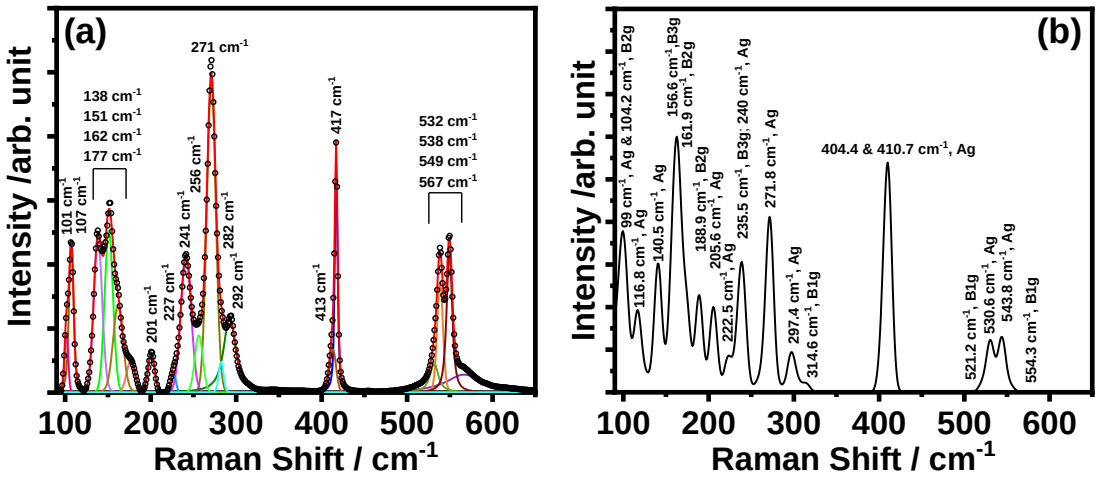

Figure 3. Raman spectroscopy of $BiPS_4$: (a) spectrum measured under near-resonant 785 nm excitation and (b) calculated modes using density functional perturbation theory on optimized crystal structures.

A characteristic Raman spectrum of $BiPS_4$ powder under 785 nm excitation is shown in **Figure 3a**. This NIR excitation produces a near-resonant Raman response, enhancing low-intensity modes through coupling with electronic transitions. Following the differences in atomic weights, the Raman signals can be divided in three frequency ranges associated with Bi (below 91 cm^{-1}), S (between 92 and 411 cm^{-1}) and P (above 500 cm^{-1}). In view of the lack of detailed analysis of $BiPS_4$ Raman spectra, we employed density functional perturbation theory to calculate the various modes within the experimentally available range as shown in **Figure 3b** (calculations over the entire spectral range are shown in **Figure S3,** while **Table S1** lists the assignment of these prominent Raman modes). The simulated spectrum allows us to deconvolute the various experimental Raman bands employing Voigt functions. As the Raman shift calculations are extremely sensitive to the crystal structure, the small shift of < +7cm^{-1} between the measured to calculated spectrum could be attributed to the difference between DFT optimized and experimental crystal structure.[12] The prominent modes at 91 cm^{-1} and 59 cm^{-1} are associated with the scissoring of Bi atoms in alternate layers in the xy-plane and along the z-axis, respectively. The modes between 92 cm^{-1} and 411 cm^{-1} are due to different vibrations of the S atoms, including rocking at 99 cm^{-1}, scissoring at 156.6 cm^{-1} and twisting at 235.5 cm^{-1}. The 271.8 cm^{-1} modes are associated with the in-plane S stretch with respect to Bi, while the sharp feature at 410 cm^{-1} is the "breathing" mode of $(PS_4)^{-3}$ S atoms. The modes above 500 cm^{-1} are due to movement of P atoms and the in-plane (xy-plane) stretch leading to 530.6 cm^{-1} and 543.8 cm^{-1} bands.

3.2 Electronic structure and optical properties. The band structure and density of states calculated using hybrid functional DFT (HSE06) are shown in **Figure 4**. The complex nature of the band edges is illustrated in **Figure 4a**, showing a high degree of degeneracy and density of states. The conduction band minimum (CBM) is located between G and X k-points while valence band minimum (VBM) is between U_0 and X at a distance of ~ 1.93 eV at 0 K, thus making the $BiPS_4$ an indirect bandgap material. However, the difference between the indirect and direct transition is only ~50 meV ($2k_BT$ at 300K), therefore optical response at the bandgap will be dominated by the direct transition. Although the temperature dependence of the bandgap has not been reported yet, the room temperature value is expected to be about 0.2 eV lower due to lattice expansion and electron-phonon coupling which have been seen in Bi-chalcogenides with similar structures.[18,25,52] The bands show a narrow dispersion and asymmetry around the CBM and VBM indicating moderate and asymmetric effective carrier masses along with the different crystallographic directions. These complex features make estimations of carrier effective masses very complicated as demonstrated by Walsh and co-workers.[53]

The diffuse reflectance spectrum of $BiPS_4$ after 90 % dilution in $BaSO_4$ is shown in **Figure 4b**. The sharp change in reflectance between 625 to 725 nm marks the fundamental band-to-band transition. The Kubelka-Munk transformation of the reflectance spectrum is performed to construct a Tauc plot assuming a direct bandgap (**Figure S4**), showing a bandgap of 1.71 eV. As far as we are aware, this is the first report of the $BiPS_4$ bandgap, which appears in close agreement with the calculated value.

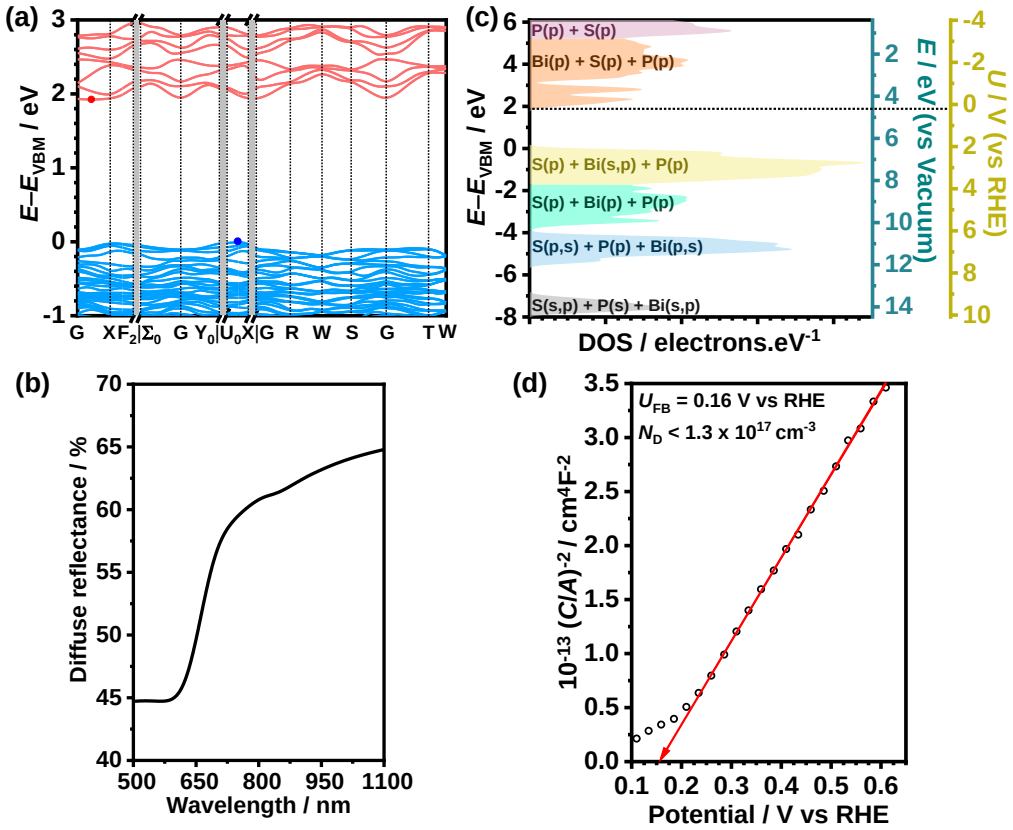

Figure 4. Electronic structure and optical properties of $BiPS_4$: (a) band structure calculated under hybrid DFT-HSE06 including spin-orbit coupling. (b) Diffuse reflectance spectrum with 90% dilution with $BaSO_4$, showing a sharp transition around 650 nm. (c) The calculated density of states highlighting the main contribution from Bi 6s, S 3p and P 3p orbitals. Elements and corresponding orbital contributions are indicated for each energy bands, appearing in order of prominence. For example, the largest contribution to the VBM is from S p-orbitals, followed by Bi s- and p-orbitals, and finally P p-orbitals. Energy values are referenced against the CBM and vacuum level, while the dotted line shows the E_F position estimated from electrochemical measurements, assuming U (RHE, V) = $q(E$ (Vacuum) + 4.44eV). (d) Mott-Schottky plot of $BiPS_4$ electrode constructed from electrochemical impedance data in Ar-saturated 0.5 M Na_2SO_4 electrolyte (pH 6.8).

As illustrated in **Figure S5**, significant relativistic effects are clearly observed in the electronic structure of $BiPS_4$ at the bottom of the conduction band. The introduction of spin-orbit coupling (SOC) affects the band structure and density of states (DOS), generating a splitting of the Bi(p) band. The inclusion SOC also causes lowering of CBM by 0.465 eV and changes the nature of fundamental transition, which are also observed in Pb-hybrid perovskites.[54] **Figure 4c** shows the calculated DOS of $BiPS_4$ and the primary elemental contributions to conduction and valence band edges. The complete ion projected orbital decomposition on the density of states as well as the band structure calculated including only scalar relativistic effects are shown in **Figure S6**. It is important to note the overlap of Bi 6s and S 3p states in the VB (around -7.5 eV and close to the VBM), with additional contribution of Bi(p) states. According to the pioneering work by Walsh and Watson,[55] these features in the electronic structure of the VB are key descriptors associated with stereochemically active Bi $6s^2$ lone-pair (see section 3.1). Furthermore, the involvement of the cation p orbitals may introduce antibonding character to the VB.

Figure 4c also shows that CBM and VBM are calculated at 4.55 and 6.48 eV, respectively, following the methodology reported by the Carter group.[51] This method consists of determining the band gap centre with respect to vacuum level from slab calculations and the band structure illustrated in **Figure 4a**. The slab-gap model involved a 50 Å slab and 20 Å gap,

cleaved at the (002) plane. This approach, however, does not take into account surface dipoles induced by interfacial charge transfer, which requires sophisticated DFT based molecular dynamics as described by Cheng and co-workers.[56] We have also estimated the band edge energies employing electrochemical capacitance measurements as described in **section S1** of the supplementary information. **Figure 4d** displays the corresponding Mott-Schottky plot featuring a well-defined linear trend over 400 mV based on the potential dependence of capacitance (**Figure S7**). The positive slope indicates n-type doping with a donor concentration of the order of 1 x 10^{17} cm^{-3}. The calculations employed a relative permittivity value of 13 (obtained from DFT) and neglected the surface roughness of the film. Interestingly, the estimated flat-band potential (U_{FB}) is 0.16 V vs RHE, which corresponds to a Fermi level E_F = 4.6 eV vs vacuum (**Figure 4c**). Considering the Boltzmann distribution and an effective density of states at the conduction band edge of 10^{19} cm^{-3}, we can estimate that the CBM is located approximately 0.1 eV above the experimental E_F. This value is remarkably close to the theoretical estimation of the CBM, suggesting that no significant interfacial dipoles are generated at the semiconductor/electrolyte junction.

Figure 5 compares the band positions of several potential Bi-absorbers against $BiPS_4$ along with some closely suitable electron and hole transport materials (ETM and HTM). It is worth noting the significantly higher ionization potential (>0.8 eV) of $BiPS_4$ compared to Bi_2S_3, despite similar bonding characteristics and a stereochemically active lone pair. Thus, one potential challenge to exploit $BiPS_4$ in a PV device would be to find a suitably aligned ETM and HTM. The band alignment of $BiPS_4$ is found to be positioned similar to BiSI. Based on **Figure 5** and our previous work on BiSI PV devices, we suggest SnO_2 and F8 may serve as a trial ETM and HTM, respectively. However, we acknowledge, like in the case of BiSI, SnO_2 can introduce an electron transport barrier and the sub-optimal alignment of F8's highest occupied molecular orbital (HOMO) level would lead to open-circuit voltage losses.

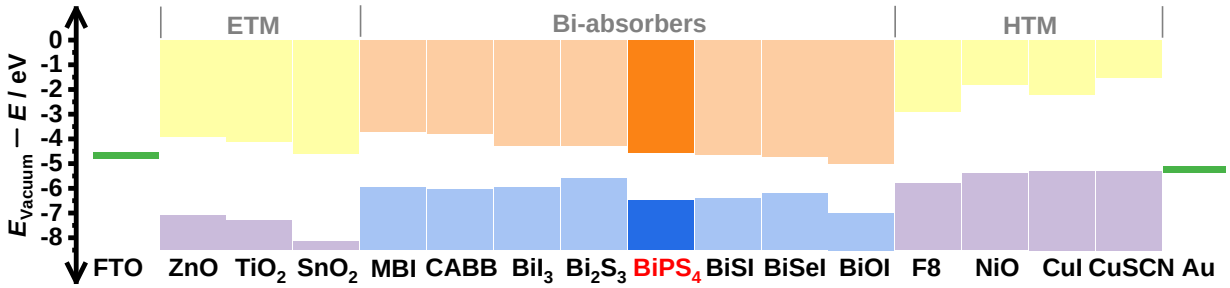

Figure 5. Comparison of band energetics of $BiPS_4$, MBI,[21] CABB,[58] BiI_3,[18] Bi_2S_3,[59] BiSI and BiSeI,[60] BiOI.[61] MBI and CABB stand for $(CH_3NH_3)_3Bi_2I_9$ and $Cs_2AgBiBr_6$, respectively. Band edge energies of the electron (ETM) and hole-transporting materials (HTM), as well as the work function of common contact, are reported in reference[57], while F8 (poly(9,9-di-n-octylfluorenyl-2,7-diyl)) is obtained from.[18,25]

3.3 Photoelectrochemical responses. A characteristic cyclic voltammogram of a $BiPS_4$ film in Ar saturated 0.1 M Na_2SO_3 solution (pH 6.5) is illustrated in **Figure 6a**. A broadening of the capacitive current is observed as the potential decreases, showing a significant charge accumulation at potentials more negative than 0.2 V vs RHE. This response indicates a transition from depletion to accumulation in the space-charge layer, in agreement with the Mott-Schottky analysis. An additional cyclic voltammogram in a wider potential range is presented in **Figure S8**. The small current increase is seen at 0.6 V vs. RHE arises from SO_3^{2-} oxidation through the pinholes in the films, leading to direct electrolyte and FTO contact. Martinez et al. have reported cyclic voltammograms over a significantly wider potential range, going deep into the accumulation regime.[62] A recent study by Stephenson et al. on BiOCl thin-film clearly showed the formation of Bi^0 as the potential is swept to the electron accumulation regime, leading to the formation Bi_2O_3 as the potential is swept back to positive potentials.[24] Based on the strong contribution of Bi orbits to the CBM, we anticipate similar degradation mechanism operating in $BiPS_4$.

Figure 6b shows the potential dependence of the photocurrent external quantum efficiency (EQE) of $BiPS_4$ at 500, 600 and 700 nm in the presence of SO_3^{2-} ion as hole acceptor. Positive photocurrents are recorded over the entire potential range, confirming the n-type nature of $BiPS_4$. The onset potential of the photocurrent is about 0.15 V vs RHE, which is close to the E_{FB} estimated from the Mott-Schottky plot (**Figure 4d**). The effective flux of minority carriers (holes) to the surface as a function of the applied can be estimated from the Gaertner equation as described in **section S1** of the supplementary information.[63] The shaded regions in **Figure 6b** show the difference between the EQE predicted by the Gaertner model and the experimental value at the various wavelengths, suggesting the presence of recombination losses which becomes more substantial towards the U_{FB}. The spectral response of the EQE measured at 0.76 V vs RHE is displayed in **Figure 6c**. The spectrum features a sharp absorption edge with onset at 720 nm, with little tailing towards longer wavelength which is a further indication of the highly crystalline nature of the powder. The bandgap of $BiPS_4$ can also be estimated from the EQE

absorption edge using a modified Tauc plot, substituting absorption coefficient by -ln(1-EQE) (see **Figure S9**).[63] We could estimate a bandgap of E_g = 1.73 eV, which is in close agreement with diffuse reflectance data.

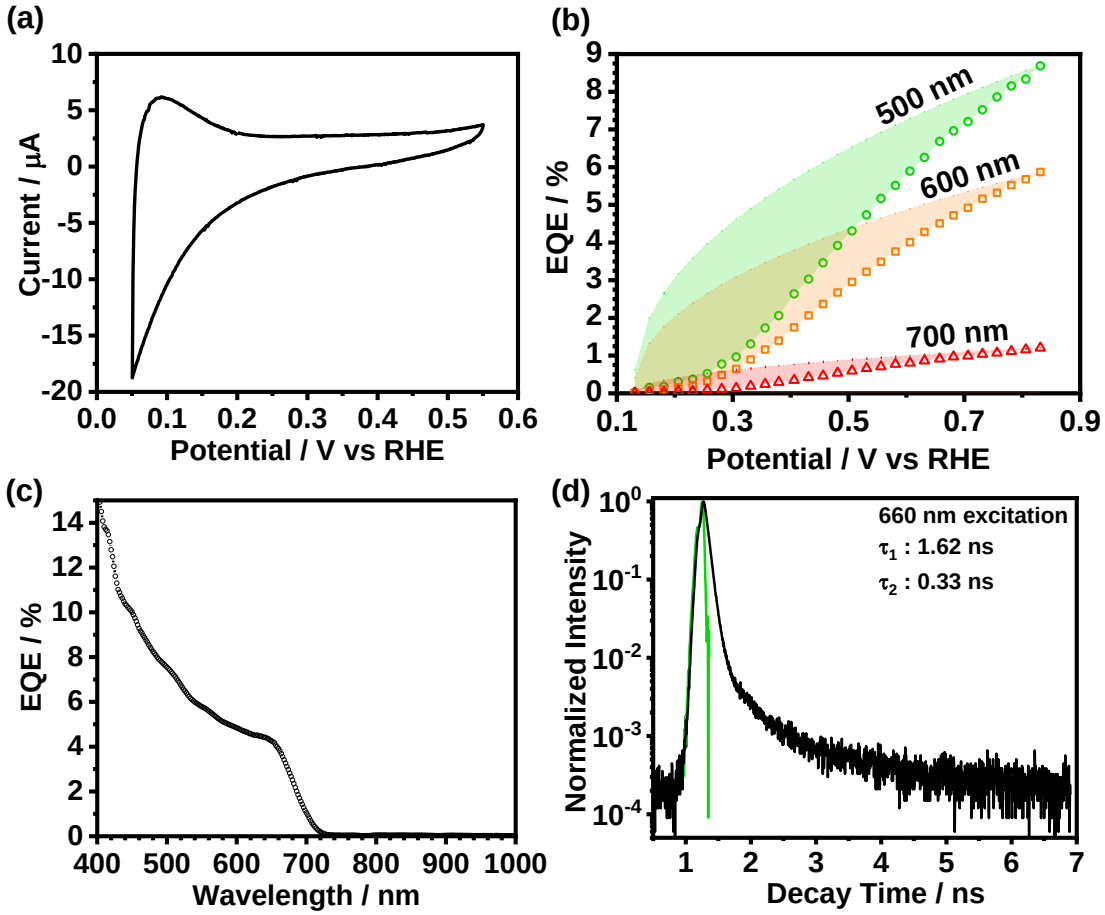

Figure 6. Photoelectrochemical and photophysical measurements of $BiPS_4$: (a) cyclic voltammogram at 100 mV/s in Ar-saturated 0.1 M Na_2SO_3 electrolyte (pH 6.5); (b) Potential dependence of EQE (symbols) and Gaertner limit (lines), highlighting the estimated losses due to interfacial recombination; (c) External quantum efficiency (EQE) spectrum measured at 0.76 V vs RHE. (d) Time-resolved photoluminescence transient at 660 nm excitation, showing a bi-exponential decay with two time-constants of 0.33 and 1.62 ns. The green trace represents the instrument response function (IRF).

The films show EQE higher than 5% at 600 nm and strongly increasing towards shorter wavelengths, suggesting that bulk recombination also plays a prominent role. **Figure 6d** shows time-resolved photoluminescence (TRPL) transient of $BiPS_4$, featuring a bi-exponential decay with carrier lifetimes of 0.33 ns and 1.62 ns. Such short carrier lifetimes introduces strong QE depends on the penetration depth of light and hence on the excitation wavelength.[64] Crucially, despite fulfilling key electronic criteria for defect-tolerance, ns carrier lifetimes indicate the presence of defect states acting as recombination centres. Indeed, recent computational studies on BiSI reported by Ganose et al., Bi_S antisites and sulfur vacancies (V_S) have been proposed as deep trap states.[65] Although atomic-resolution TEM image (**Figure 2b**) shows little evidence of Bi disorder, V_S are extremely challenging to visualize. The structural disorder also manifests itself as the so-called Urbach tails (E_U) which can be estimated from sub-bandgap responses close to the band edge as illustrated in **Figure S10**. The value estimated for $BiPS_4$ (26 meV) is significantly smaller than those obtained for BiI_3 (91 meV) and BiSI (222 meV) thin films featuring power conversion efficiencies in the range of 1.2-1.8 %.[18,25] High-efficiency absorbers such as Si, GaAs, CdTe, Cu(In,Ga)Se_2 and Pb-hybrid perovskites feature smaller E_U values (< 20 meV),[66] highlighting the need of more comprehensive studies of defects in Bi-based materials.

4. Conclusion

This study provides the first detailed study of $BiPS_4$ crystals as potential Earth-abundant solar absorber. The large Bi ionic radius introduces a rather unusual crystal structure which neither matches the layered structure of thiophosphites[62] nor the to that of thiophosphates of Group III cations (B, Al, In, Ga)[22,67–69]. $BiPS_4$ rather forms an unusual 3-dimensional orthorhombic structure with two different distorted Bi coordination sites as a result of the $6s^2$ lone-pairs, which is similar to the bonding in orthorhombic Bi_2S_3.[70] The $BiPS_4$ structure was also confirmed by the close correlation between experimental Raman spectra recorded under near-resonant conditions and computed Raman modes employing Density Functional Perturbation Theory. Band structure calculations show a significant contribution of spin-orbit coupling introduced by Bi 6p orbitals on the energy and dispersion of the CBM. The strong mixing of Bi and S orbitals in the valence band is also a key observation connected to the structural distortion induced by the Bi $6s^2$ lone pairs. The computed band gap closely matches the optical responses which are dominated by a direct transition at 1.72 eV. Electrochemical experiments revealed n-type conductivity with a flat band potential located at 0.16 V vs RHE. A strong potential and wavelength dependence of the photoelectrochemical external quantum yield in the presence of SO_3^{2-} as hole-scavenger suggested limited carrier lifetimes, which was confirmed by time-resolved PL measurements. Further studies are required in order to elucidate the nature of recombination sites, including modelling intrinsic defects and to devise synthetic strategies for improving the carrier collection.

ASSOCIATED CONTENT

Supporting Information

The Supporting Information is available free of charge via the Internet at http://pubs.acs.org. Details of electrochemical analysis calculated electronic structures without spin-orbit coupling (SOC) and comparison with electronic structure calculated with SOC, Tauc plot for bandgap estimation from diffuse reflectance measurements, potential dependence of capacitance, and Tauc plot for bandgap estimation from the spectral response of quantum efficiency measurement.

AUTHOR INFORMATION

Notes

The authors declare no competing financial interest

All data presented in this article can be freely accessed from Bristol's Research Data Repository ().

Corresponding Author

*Email: david.fermin@bristol.ac.uk

ORCID

Devendra Tiwari: 0000-0001-8225-0000

Dominic Alibhai: 0000-0001-5421-4424

David Cherns: 0000-0002-5419-5486

David J Fermin: 0000-0002-0376-5506

Acknowledgement

DT and DJF are both thankful to UK Engineering and Physical Sciences Research Council, EPSRC) the PVTEAM grant (EP/L017792/1). The first-principles calculations are facilitated by high-performance computing facility at the Advanced Computing Research Centre, University of Bristol (www.bris.ac.uk/acrc/). The instrumentation for electron microscopy and impedance spectroscopy were procured through by EPSRC Capital grant (EP/ K035746/1). We are also grateful to Wolfson Bioimaging Facility at the University of Bristol for fluorescence lifetime imaging microscopy (FLIM) BBSRC/EPSRC-funded Synthetic Biology Research Centre grant: L01386X. Authors would also like to acknowledge Dr Ian Griffiths, University of Oxford, for use of the South of England Analytical Electron Microscope (JEOL ARM200F), and assistance in obtaining the HAADF image in Figure 2.

References

(1) Giustino, F.; Snaith, H. J. Toward Lead-Free Perovskite Solar Cells. *ACS Energy Lett.* **2016**, *1*, 1233–1240.

(2) Kamat, P. V.; Bisquert, J.; Buriak, J. Lead-Free Perovskite Solar Cells. *ACS Energy Lett.* **2017**, *2*, 904–905.

(3) Miller, N. C.; Bernechea, M. Research Update: Bismuth Based Materials for Photovoltaics. *APL Mater.* **2018**, *6*, 084503-1–12.

(4) Ganose, A. M.; Savory, C. N.; Scanlon, D. O. Beyond Methylammonium Lead Iodide: Prospects for the Emergent Field of Ns^2 Containing Solar Absorbers. *Chem. Commun.* **2017**, *53*, 20–44.

(5) Ollevier, T. New Trends in Bismuth-Catalyzed Synthetic Transformations. *Org. Biomol. Chem.* **2013**, *11*, 2740–2755.

(6) He, R.; Xu, D.; Cheng, B.; Yu, J.; Ho, W. Review on Nanoscale Bi-Based Photocatalysts. *Nanoscale Horizons* **2018**, *3*, 464–504.

(7) Osterhage, H.; Gooth, J.; Hamdou, B.; Gwozdz, P.; Zierold, R.; Nielsch, K. Thermoelectric Properties of Topological Insulator Bi_2Te_3, Sb_2Te_3, and Bi_2Se_3 Thin Film Quantum Wells. *Appl. Phys. Lett.* **2014**, *105*, 123117-1–5.

(8) Zhang, H.; Liu, C. X.; Qi, X. L.; Dai, X.; Fang, Z.; Zhang, S. C. Topological Insulators in Bi_2Se_3, Bi_2Te_3 and Sb_2Te_3 with a Single Dirac Cone on the Surface. *Nat. Phys.* **2009**, *5*, 438–442.

(9) Alva, V.; Saleh, O.; Lupas, A. N.; Heide, L.; Yang, H.; Chi, N. C. N.; Dallner, G.; Andersson, B.; Ernster, L.; Appelkvist, E. L.; et al. Switchable Ferroelectric Diode and Photovoltaic Effect in $BiFeO_3$. *Science (80-.).* **2014**, *343*, 881–886.

(10) Song, J.; Yuan, J.; Xia, F.; Liu, J.; Zhang, Y.; Zhong, Y. L.; Zheng, J.; Liu, Y.; Li, S.; Zhao, M.; et al. Large-Scale Production of Bismuth Chalcogenide and Graphene Heterostructure and Its Application for Flexible Broadband Photodetector. *Adv. Electron. Mater.* **2016**, *2*, 1600077-1–9.

(11) Sleight, A. W. Bismuthates: $BaBiO_3$ and Related Superconducting Phases. *Phys. C Supercond. its Appl.* **2015**, *514*, 152–165.

(12) Bernechea, M.; Miller, N. C.; Xercavins, G.; So, D.; Stavrinadis, A.; Konstantatos, G. Solution-Processed Solar Cells Based on Environmentally Friendly $AgBiS_2$ Nanocrystals. *Nat. Photonics* **2016**, *10*, 521–525.

(13) Wang, J. J.; Akgul, M. Z.; Bi, Y.; Christodoulou, S.; Konstantatos, G. Low-Temperature Colloidal Synthesis of $CuBiS_2$ Nanocrystals for Optoelectronic Devices. *J. Mater. Chem. A* **2017**, *5*, 24621–24625.

(14) Hamdeh, U. H.; Nelson, R. D.; Ryan, B. J.; Bhattacharjee, U.; Petrich, J. W.; Panthani, M. G. Solution-Processed BiI_3 Thin Films for Photovoltaic Applications: Improved Carrier Collection via Solvent Annealing. *Chem. Mater.* **2016**, *28*, 6567–6574.

(15) Lehner, A. J.; Wang, H.; Fabini, D. H.; Liman, C. D.; Hébert, C. A.; Perry, E. E.; Wang, M.; Bazan, G. C.; Chabinyc, M. L.; Seshadri, R. Electronic Structure and Photovoltaic Application of BiI_3. *Appl. Phys. Lett.* **2015**, *107*, 131109-1–5.

(16) Sansom, H. C.; Whitehead, G. F. S.; Dyer, M. S.; Zanella, M.; Manning, T. D.; Pitcher, M. J.; Whittles, T. J.; Dhanak, V. R.; Alaria, J.; Claridge, J. B.; et al. $AgBiI_4$ as a Lead-Free Solar Absorber with Potential Application in Photovoltaics. *Chem. Mater.* **2017**, *29*, 1538–1549.

(17) Kim, Y.; Yang, Z.; Jain, A.; Voznyy, O.; Kim, G. H.; Liu, M.; Quan, L. N.; García de Arquer, F. P.; Comin, R.; Fan, J. Z.; et al. Pure Cubic-Phase Hybrid Iodobismuthates $AgBi_2I_7$ for Thin-Film Photovoltaics. *Angew. Chemie - Int. Ed.* **2016**, *55*, 9586–9590.

(18) Tiwari, D.; Alibhai, D.; Fermin, D. J. Above 600 MV Open-Circuit Voltage BiI_3 Solar Cells. *ACS Energy Lett.* **2018**, *3*, 1882–1886.

(19) Lee, L. C.; Huq, T. N.; Macmanus-Driscoll, J. L.; Hoye, R. L. Z. Research Update: Bismuth-Based Perovskite-Inspired Photovoltaic Materials. *APL Mater.* **2018**, *6*, 084502-1–16.

(20) Bai, F.; Hu, Y.; Hu, Y.; Qiu, T.; Miao, X.; Zhang, S. Lead-Free, Air-Stable Ultrathin $Cs_3Bi_2I_9$ Perovskite Nanosheets for Solar Cells. *Sol. Energy Mater. Sol. Cells* **2018**, *184*, 15–21.

(21) Zhang, Z.; Li, X.; Xia, X.; Wang, Z.; Huang, Z.; Lei, B.; Gao, Y. High-Quality $(CH_3NH_3)_3Bi_2I_9$ Film-Based Solar Cells: Pushing Efficiency up to 1.64%. *J. Phys. Chem. Lett.* **2017**, *8*, 4300–4307.

(22) Bubenzer, A.; Nitsche, R.; Raufer, A. Vapour Growth and Piezoelectric Effect of Indium Thiophosphate, $InPS_4$. *J. Cryst. Growth* **1975**, *29*, 237–240.

(23) Hoye, R. L. Z.; Lee, L. C.; Kurchin, R. C.; Huq, T. N.; Zhang, K. H. L.; Sponseller, M.; Nienhaus, L.; Brandt, R. E.; Jean, J.; Polizzotti, J. A.; et al. Strongly Enhanced Photovoltaic Performance and Defect Physics of Air-Stable Bismuth Oxyiodide (BiOI). *Adv. Mater.* **2017**, *29*, 1702176-1–10.

(24) Stephenson, J.; Celorrio, V.; Tiwari, D.; Hall, S. R.; Green, D. C.; Fermín, D. J. Photoelectrochemical Properties of BiOCl Microplatelets. *J. Electroanal. Chem.* **2018**, *819*, 171–177.

(25) Tiwari, D.; Cardoso-Delgado, F.; Alibhai, D.; Mombrú, M.; Fermín, D. J. Photovoltaic Performance of Phase-Pure Orthorhombic BiSI Thin-Films. *ACS Appl. Energy Mater.* **2019**, *2*, 3878–3885.

(26) Tiwari, D.; Fermin, D. J.; Chaudhuri, T. K.; Ray, A. Solution Processed Bismuth Ferrite Thin Films for All-Oxide Solar Photovoltaics. *J. Phys.*

Chem. C **2015**, *119*, 5872–5877.

(27) Du, K. Z.; Wang, X. Z.; Liu, Y.; Hu, P.; Utama, M. I. B.; Gan, C. K.; Xiong, Q.; Kloc, C. Weak Van Der Waals Stacking, Wide-Range Band Gap, and Raman Study on Ultrathin Layers of Metal Phosphorus Trichalcogenides. *ACS Nano* **2016**, *10*, 1738–1743.

(28) Odoulov, S. G.; Shumelyuk, A. N.; Brost, G. A.; Magde, K. M. Enhancement of Beam Coupling in the near Infrared for Tin Hypothiodiphosphate. *Appl. Phys. Lett.* **1996**, *69*, 3665–3667.

(29) Bourdon, X.; Maisonneuve, V.; Cajipe, V. B.; Payen, C.; Fischer, J. E. Copper Sublattice Ordering in Layered $CuMP_2Se_6$ (M=In, Cr). *J. Alloys Compd.* **1999**, *283*, 122–127.

(30) Misuryaev, T. V.; Murzina, T. V.; Aktsipetrov, O. A.; Sherstyuk, N. B.; Cajipe, V. B.; Bourdon, X. Second Harmonic Generation in the Lamellar Ferrielectric $CuInP_2S_6$. *Solid State Commun.* **2000**, *115*, 605–608.

(31) Kroupa, J.; Tyagur, Y. I.; Grabar, A. A.; Vysochanskii, Y. M. Electro-Optic Properties of $Sn_2P_2S_6$. *Ferroelectrics* **1999**, *223*, 421–430.

(32) McCarthy, T. J.; Kanatzidis, M. G. Synthesis in Molten Alkali Metal Polyselenophosphate Fluxes: A New Family of Transition Metal Selenophosphate Compounds, $A_2MP_2Se_6$ (A = K, Rb, Cs; M = Mn, Fe) and $A_2M'_2P_2Se_6$ (A = . *Inorg. Chem.* **1995**, *34*, 1257–1267.

(33) Chondroudis, K.; Kanatzidis, M. G. Group 10 and Group 12 One-Dimensional Selenodiphosphates:$A_2MP_2Se_6$(A=K, Rb, Cs;M=Pd, Zn, Cd, Hg). *J. Solid State Chem.* **1998**, *138*, 321–328.

(34) Frindt, R. F.; Yang, D.; Westreich, P. Exfoliated Single Molecular Layers of $Mn_{0.8}PS_3$ and $Cd_{0.8}PS_3$. *J. Mater. Res.* **2005**, *20*, 1107–1112.

(35) Takano, Y.; Arai, N.; Arai, A.; Takahashi, Y.; Takase, K.; Sekizawa, K. Magnetic Properties and Specific Heat of MPS_3 (M = Mn, Fe, Zn). *J. Magn. Magn. Mater.* **2004**, *272–276*, e593–e595.

(36) Kuo, C. T.; Neumann, M.; Balamurugan, K.; Park, H. J.; Kang, S.; Shiu, H. W.; Kang, J. H.; Hong, B. H.; Han, M.; Noh, T. W.; et al. Exfoliation and Raman Spectroscopic Fingerprint of Few-Layer $NiPS_3$ Van Der Waals Crystals. *Sci. Rep.* **2016**, *6*, 20904-1–10.

(37) Iordanidis, L.; Bilc, D.; Mahanti, S. D.; Kanatzidis, M. G. Impressive Structural Diversity and Polymorphism in the Modular Compounds ABi_3Q_5 (A = Rb, Cs; Q = S, Se, Te). *J. Am. Chem. Soc.* **2003**, *125*, 13741–13752.

(38) Seshadri, R. Visualizing Lone Pairs in Compounds Containing Heavier Congeners of the Carbon and Nitrogen Group Elements. *Proc. Indian Acad. Sci. Chem. Sci.* **2001**, *113*, 487–496.

(39) Walsh, A.; Payne, D. J.; Egdell, R. G.; Watson, G. W. Stereochemistry of Post-Transition Metal Oxides: Revision of the Classical Lone Pair Model. *Chem. Soc. Rev.* **2011**, *40*, 4455–4463.

(40) Iwao, K.; Wuensch, B. J. The Crystal Structure of Gladite , $PbCuBi_5S_9$, a Superstructure Intermediate in the Series. *Acta Crystallogr. Sect. B Struct. Crystallogr. Cryst. Chem.* **1976**, *B32*, 2401–2409.

(41) McCarthy, T. J.; Ngeyi, S. P.; Liao, J. H.; DeGroot, D. C.; Hogan, T.; Kannewurf, C. R.; Kanatzidis, M. G. Molten Salt Synthesis and Properties of Three New Solid-State Ternary Bismuth Chalcogenides, β-$CsBiS_2$, γ-$CsBiS_2$, and $K_2Bi_8Se_{13}$. *Chem. Mater.* **1993**, *5*, 331–340.

(42) Iordanidis, L.; Schindler, J. L.; Kannewurf, C. R.; Kanatzidis, M. G. $ALn_{1\pm x}Bi_{4\pm x}S_8$(A=K,Rb;Ln=La,Ce,Pr,Nd): New Semiconducting Quaternary Bismuth Sulfides. *J. Solid State Chem.* **1999**, *143*, 151–162.

(43) Galdámez, A.; Manríquez, V.; Kasaneva, J.; Avila, R. E. Synthesis, Characterization and Electrical Properties of Quaternary Selenodiphosphates: AMP_2SE_6 with A = Cu, Ag and M = Bi, Sb. *Mater. Res. Bull.* **2003**, *38*, 1063–1072.

(44) Gave, M. A.; Weliky, D. P.; Kanatzidis, M. G. New Potassium Bismuth Thiophosphates Including the Modulated $K_{1.5}Bi_{2.5}(PS_4)_3$. *Inorg. Chem.* **2007**, *46*, 11063–11074.

(45) Zimmermann, H.; Carpentier, C. D.; Nitsche, R. The Crystal Structure of Bismuth Thiophosphate $BiPS_4$. *Acta Crystallogr. Sect. B Struct. Crystallogr. Cryst. Chem.* **1975**, *31*, 2003–2006.

(46) Nitsche, R.; Wild, P. Crystal Growth of Metal-Phosphorus-Sulfur Compounds by Vapor Transport. *Mater. Res. Bull.* **1970**, *5*, 419–423.

(47) Clark, S. J.; Segall, M. D.; Pickard, C. J.; Hasnip, P. J.; Probert, M. I. J.; Refson, K.; Payne, M. C. First Principles Methods Using CASTEP. *Zeitschrift fur Krist.* **2005**, *220*, 567–570.

(48) Payne, M. C.; Teter, M. P.; Allan, D. C.; Arias, T. A.; Joannopoulos, J. D. Iterative Minimization Techniques for Ab Initio Total-Energy Calculations: Molecular Dynamics and Conjugate Gradients. *Rev. Mod. Phys.* **1992**, *64*, 1045–1097.

(49) Grimme, S. Semiempirical GGA-Type Density Functional Constructed with a Long-Range Dispersion Correction. *J. Comput. Chem.* **2006**, *27*, 1787–1799.

(50) Lenthe, E. Van; Baerends, E. J.; Snijders, J. G.; Lenthe, E. Van; Baerends, E. J.; Snijders, J. G. Relativistic Regular Twocomponent Hamiltonians Relativistic Regular Two-Component Hamiltonians. *J. Chem. Phys.* **1993**, *99*, 4597–4610.

(51) Toroker, M. C.; Kanan, D. K.; Alidoust, N.; Isseroff, L. Y.; Liao, P.; Carter, E. A. First Principles Scheme to Evaluate Band Edge Positions in Potential Transition Metal Oxide Photocatalysts and Photoelectrodes. *Phys. Chem. Chem. Phys.* **2011**, *13*, 16644–16654.

(52) Gildart, L.; Kline, J. M.; Mattox, D. M. Some Semiconducting Properties of Bismuth Trisulfide. *J. Phys. Chem. Solids* **1961**, *18*, 286–289.

(53) Whalley, L. D.; Frost, J. M.; Morgan, B. J.; Walsh, A. Impact of Nonparabolic Electronic Band Structure on the Optical and Transport Properties of Photovoltaic Materials. *Phys. Rev. B* **2019**, *99*, 085207-1–11.

(54) Frost, J. M.; Butler, K. T.; Brivio, F.; Hendon, C. H.; Van Schilfgaarde, M.; Walsh, A. Atomistic Origins of High-Performance in Hybrid Halide Perovskite Solar Cells. *Nano Lett.* **2014**, *14*, 2584–2590.

(55) Walsh, A.; Watson, G. W. Influence of the Anion on Lone Pair Formation in Sn(II) Monochalcogenides: A DFT Study. *J. Phys. Chem. B* **2005**, *109*, 18868–18875.

(56) Le, J.; Iannuzzi, M.; Cuesta, A.; Cheng, J. Determining Potentials of Zero Charge of Metal Electrodes versus the Standard Hydrogen Electrode from Density-Functional-Theory-Based Molecular Dynamics. *Phys. Rev. Lett.* **2017**, *119*, 016801-1–6.

(57) Chueh, C. C.; Li, C. Z.; Jen, A. K. Y. Recent Progress and Perspective in Solution-Processed Interfacial Materials for Efficient and Stable Polymer and Organometal Perovskite Solar Cells. *Energy Environ. Sci.* **2015**, *8*, 1160–1189.

(58) Greul, E.; Petrus, M. L.; Binek, A.; Docampo, P.; Bein, T. Highly Stable, Phase Pure $Cs_2AgBiBr_6$ Double Perovskite Thin Films for Optoelectronic Applications. *J. Mater. Chem. A* **2017**, *5*, 19972–19981.

(59) Han, D.; Du, M. H.; Dai, C. M.; Sun, D.; Chen, S. Influence of Defects and Dopants on the Photovoltaic Performance of Bi_2S_3: First-Principles Insights. *J. Mater. Chem. A* **2017**, *5*, 6200–6210.

(60) Ganose, A. M.; Butler, K. T.; Walsh, A.; Scanlon, D. O. Relativistic Electronic Structure and Band Alignment of BiSI and BiSeI: Candidate Photovoltaic Materials. *J. Mater. Chem. A* **2016**, *4*, 2060–2068.

(61) Ganose, A. M.; Cuff, M.; Butler, K. T.; Walsh, A.; Scanlon, D. O. Interplay of Orbital and Relativistic Effects in Bismuth Oxyhalides: BiOF, BiOCl, BiOBr, and BiOI. *Chem. Mater.* **2016**, *28*, 1980–1984.

(62) Mayorga-Martinez, C. C.; Sofer, Z.; Sedmidubský, D.; Huber, Š.; Eng, A. Y. S.; Pumera, M. Layered Metal Thiophosphite Materials: Magnetic, Electrochemical, and Electronic Properties. *ACS Appl. Mater. Interfaces* **2017**, *9*, 12563–12573.

(63) Peat, R.; Peter, L. M. Determination of the Electron Diffusion Length in P-GaP by Intensity Modulated Photocurrent Measurements with an Electrolyte Contact. *Appl. Phys. Lett.* **1987**, *51*, 328–330.

(64) Nelson, R. J.; Sobers, R. G. Minority-Carrier Lifetimes and Internal Quantum Efficiency of Surface-Free GaAs. *J. Appl. Phys.* **1978**, *49*, 6103–6108.

(65) Ganose, A. M.; Matsumoto, S.; Buckeridge, J.; Scanlon, D. O. Defect Engineering of Earth-Abundant Solar Absorbers BiSI and BiSeI. *Chem. Mater.* **2018**, *30*, 3827–3835.

(66) Jean, J.; Mahony, T. S.; Bozyigit, D.; Sponseller, M.; Holovský, J.; Bawendi, M. G.; Bulović, V. Radiative Efficiency Limit with Band Tailing Exceeds 30% for Quantum Dot Solar Cells. *ACS Energy Lett.* **2017**, *2*, 2616–2624.

(67) Peter, B.; Carpentier, C. D. The Crystal Structure of Gallium Thiophosphate, $GaPS_4$. *Acta Cryst.* **1973**, *B29*, 1864–1868.

(68) Weiss, V. A.; Schäfer, H. Zur Kenntnis von Bortetrathiophosphat BPS_4. *Z. Naturforschg.* **1963**, *18b*, 81–82.

(69) Kuhn, A.; Eger, R.; Ganter, P.; Duppel, V.; Nuss, J.; Lotsch, B. V. In Search of Aluminum Hexathiohypodiphosphate: Synthesis and Structures of Ht-$AlPS_4$, Lt-$AlPS_4$, and $Al_4(P_2S_6)_3$. *Zeitschrift fur Anorg. und Allg. Chemie* **2014**, *640*, 2663–2668.

(70) Kupčík, V.; Veselá-Nováková, L. Zur Kristallstruktur Des Bismuthinits, Bi_2S_3. *Tschermaks Mineral. und Petrogr. Mitteilungen* **1970**, *14*, 55–59.

For Table of Contents Only